Aerosol Jet® Printing of functionally graded SOFC anode interlayer and microstructural investigation by low voltage scanning electron microscopy

Mary Sukeshini A. [a,c,*], Frederick Meisenkothen [b], Paul Gardner [c], Thomas L. Reitz [c]

[a] University of Dayton Research Institute, Dayton, OH 45469, USA
[b] UES Corp., Dayton, OH 45432, USA
[c] The Air Force Research Laboratory, Wright-Patterson AFB, OH 45433, USA

HIGHLIGHTS

► Aerosol jet printing, a new method used for solid oxide fuel cells fabrication.
► Printed porous anode interlayer with compositional grading and dense electrolyte.
► Cells with graded interlayer performed better than cells with non-graded interlayers.
► Printed layers had highly reproducible microstructure and electrochemical performance.
► Low voltage scanning electron microscopy clearly distinguished Ni, YSZ and pores.

ARTICLE INFO

ABSTRACT

Yttria-stabilized zirconia (YSZ) electrolyte and functionally graded anode interlayers with compositional variation were deposited by Aerosol Jet® Printing (AJP) using ink suspensions of NiO and YSZ. The AJP system's dual atomizer configuration that allows on-demand material mixing was used to deposit the graded composite anode interlayer. These layers together with an LSM (strontium doped lanthanum manganite) based pasted cathode layer were integrated in an anode supported SOFC button cell. Cells with graded anode interlayers performed better than cells with a non-graded anode interlayer. The enhancement in electrochemical performance can be attributed to the compositional gradation. The current printing method of fabricating SOFC layers shows clear advantages of high reproducibility. In routine SEM (scanning electron microscopy) evaluation of microstructures, acceleration voltages typically used are 10–20 kV. Due to the similar backscattering coefficients of YSZ and Ni, it is difficult to clearly distinguish between the two phases in the image. In this work, low accelerating voltages (<5 kV) were used to introduce a divergence of the YSZ and Ni backscatter coefficients to investigate the composite layers printed. The backscattering mechanism for image contrast was confirmed and clarified by specially designed SEM experiments that isolated BSE (back scattered electrons) from SE (secondary electrons).

1. Introduction

Solid oxide fuel cells (SOFCs) have attracted the attention of researchers globally owing to the technological advantages of high efficiency, low emissions, fuel flexibility, and their suitability for combined heat and power applications [1–3]. SOFC electrodes, electrolytes and functional/buffer layer components can be fabricated through a variety of routes [4]. Several approaches [5] ranging from physical/chemical/electrochemical methods to wet ceramic methods that include rf magnetron sputtering [6–8], pulsed-laser deposition [9], plasma spray [10–12], electrochemical vapor deposition [13], tape casting [14,15], screen printing [16], dip coating [17], wet powder spraying [18], sol–gel [19] and colloidal deposition [20] have been employed to deposit layers ranging in thickness from sub microns to tens of microns. Physical methods such as sputtering and pulsed laser provide fine thickness control but are not practical approaches for scale up from a cost perspective. These methods are most suited for creating model electrodes that are sub micrometer in thickness for fundamental studies. Commonly used wet ceramic methods such as screen printing, tape casting and dip coating typically used for thick layers, while simple, are limiting due to the difficulties in obtaining reproducible uniformity. The problem of precise calibration of the material and

squeegee to ensure uniform thickness in the case of screen printing and the problem of layer by layer drying in dip coating limit the scale up of these popular methods. Direct write methods based on inkjet printing is gaining momentum as a potential manufacturing method for SOFC fabrication. The relative ease of thickness control, ability to pattern without the need for masking procedures and reproducibility of microstructures make this method quite attractive [21–26] for multilayer configurations.

More recently, another method of direct write based on aerodynamic focusing of aerosolized ink droplets called Aerosol Jet® Printing (AJP) has been explored [27,28] for SOFC fabrication. This type of direct-write approach offers further advantages over traditional methods in that it can allow functional gradation of layer composition providing the potential for improved cell design flexibility which may permit performance not possible with conventional processing methodologies. Typical advantages of AJP include fine write control enabling precise deposition of micron-sized features and patterning of films without the use of a mask as well as the capability of conformal printing [29] and high material utilization. These advantages can be effectively exploited for fabrication of all non-supporting SOFC components including electrolyte, electrodes and interconnects. In our previous reports [27,28] we reported the aerosol jet printing of electrolyte (dense) and composite cathode layers (porous) onto anode supported button cells and demonstrated electrochemical performance consistent with that produced by other approaches. In this work we explore the potential to functionally grade the anode interlayer in terms of composition. Functionally graded anode and cathode interlayers with compositional or porosity variation are commonly used in SOFCs. Hart et al. [30] have shown improved cathode performance with grading. Functional gradation based on variation of composition in the interlayers/electrodes has two typical advantages of reduction of stresses due to thermal mismatch, and optimization of the ionic and electronic conductive networks. The primary focus of the current work is to explore the potential for printing porous composite anode layers with compositional gradation using aerosol jet printing, and use an effective diagnostic tool to examine the printed microstructures. To assess the microstructure of the printed components of electrolyte and graded composite interlayer, a less widely used but very effective method of *low voltage* scanning electron microscopy has been employed to clearly distinguish the different phases of Ni-percolating and non-percolating, YSZ, and pores.

2. Experimental

2.1. Functionally graded anode interlayer

2.1.1. NiO and YSZ ink preparation and characterization

Yttria doped stabilized zirconia (8 mol% YSZ Tosoh, TZ-8YS) was used as the active material for the YSZ ink. NiO (J.T. Baker) was used as the active material for NiO ink suspension. The starting powders YSZ and NiO were characterized by measuring their multi-point BET (Brunauer–Emmett–Teller) surface area using ASAP 2020 automatic physisorption analyzer (Micromeritics Instrument Corp., Norcross, GA). Nitrogen was used as the adsorption gas. The samples were desorbed at 300 °C for 3 h before measurement. For the composite anode interlayers of NiO/YSZ, two separate inks based on NiO and YSZ were prepared. The solvent used was a combination of 2-butanol and α-terpineol. A copolymer with acidic groups, Disperbyk-111 (BYK additives and instruments) was used as dispersant. Polyvinyl butyral (PVB), butyl benzyl phthalate (BBP), and polyalkylene glycol (PAG) and ethyl cellulose (EC) were utilized as binder and plasticizer constituents. Inks were prepared by the addition of powders, to the combination of solvents

containing the dispersant. This suspension was ball milled for a few hours. To this milled suspension, binders and plasticizers were added and again ball milled over night using 5 mm diameter zirconia milling beads. The solids loading for both, YSZ for the electrolyte ink and YSZ and NiO for interlayer ink was 34.7 wt% each. Viscosity measurements for the ink formulations were made using a Rheolab QC rheometer (Anton-Paar). More details about ink preparation/composition are presented in Ref. [27].

2.1.2. Deposition process, deposition rate of NiO and YSZ and mass calibration curves

2.1.2.1. *Dual atomizer configuration.* The AJP M³D® (Maskless Mesoscale Materials Deposition, Optomec Inc., Albuquerque) system's dual atomizer configuration is depicted as a schematic in Fig. 1. As can be seen in Fig. 1, the design allows on-demand material mixing. Instead of the traditional dry mixing/ball milling of the composite materials, here the individually aerosolized inks are mixed together on the fly as they enter the deposition head. Two complete Pneumatic Atomizer Virtual Impactor (PAVI) units feed into a "Y" connector and then into the nozzle head. The two units can be independently controlled such that simultaneous or individual use is possible allowing for single component or composite layer deposition. Suitable gas flow (for atomizer, exhaust and sheath) conditions for the two components, NiO and YSZ were selected such that the two individual atomizers were simultaneously operated to output any desired ratio of the two components dictated by the maximum and minimum deposition rate of the individual component materials. Details of the atomization process and definitions of atomizer, exhaust and sheath gas are provided in section 2.1.2.2 below.

2.1.2.2. *Pneumatic atomization and deposition process.* In the pneumatic atomization process (refer individual atomizer in Fig. 1), compressed gas is expanded through the atomizer nozzle, producing a high-velocity jet. As a result of the Bernoulli effect, ink,
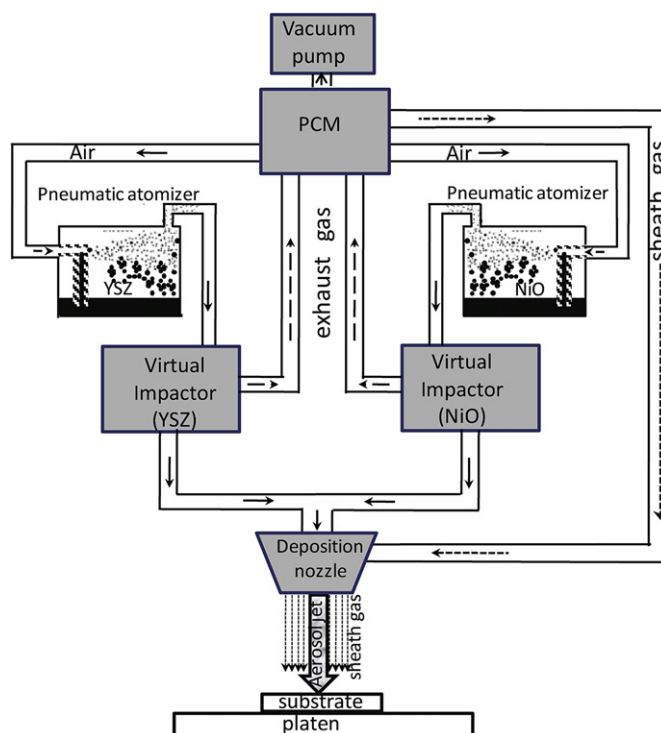

Fig. 1. Schematic of aerosol jet printer with the dual atomizer configuration.

paste, or other material is drawn from the reservoir into the atomizer nozzle. Subsequently, the high-velocity jet breaks the liquid stream into droplets that are then suspended in the flow. The high-velocity gas stream, including suspended droplets, exits the nozzle and impinges on the sidewalls of the atomizer reservoir. Large droplets impact on the sidewalls of the reservoir and drain back into it while smaller particles remain suspended in the gas. The gas flow rates necessary to form the high velocity jet are too high to be used with the M³D® deposition head and must be reduced. Simply bleeding off gas is inefficient, since atomized material would be lost. A virtual impactor is used to reduce the gas flow rate while minimizing the amount of atomized material lost during flow reduction. At the deposition head, a sheath gas surrounds the aerosol jet and prevents contact with the nozzle wall and aids in focusing the aerosol beam. In the current study, dried air was used as atomizer, exhaust and sheath gas.

2.1.2.3. Method for composition selection − mass calibration curves. In order to select a particular composition of the composite for the material mixing, the deposition rates of the individual constituents have to be first determined. Profiles of deposition rate as a function of atomizing/exhaust conditions called mass calibration curves have to be established, i.e., determine the deposition rates for the individual component as a function of the atomizing condition. Typically, for a fixed atomizing gas flow rate, determine the deposited amount as a function of exhaust gas flow rate for a pre-set sheath gas flow. Repeat this at different atomizing flow rate. With the knowledge of the individual deposition rate and their corresponding gas flow conditions, a matrix of compositions is obtained. From this matrix, the gas flow conditions are chosen for the desired compositions in the composite for mixing the two materials on the fly.

2.1.3. Printing of compositionally graded NiO/YSZ interlayer

The substrate for printing was a commercially supplied laminated green tape about 700 μm in thickness and having a composition of 55 wt% NiO/45 wt% YSZ. The anode support substrate was initially bisque fired at 950 °C in order to drive off solvents from tape casting, as well as impart mechanical integrity. The substrates were held in position by vacuum suction on the deposition platen. The platen was kept at room temperature (*ca.* 23 °C). The substrates were divided into two identical two sets, set-1 and set-2. Each identical set had 2 different types, type-1 (non-graded) and type-2 (graded) of NiO/YSZ interlayer profiles as shown schematically in Fig. 2. Following the method described in Section 2.1.2.3, suitable gas flow conditions were chosen for the atomization of individual inks such that the desired wet compositions *x* wt% NiO/(100 − *x*) wt % YSZ shown in Fig. 2 were printed as layers. Type 1 had 12 print passes of a 50/50 wt% NiO/YSZ and type 2 had a total of 12 print

passes with functional gradation in composition along the *z*-axis. The first 4 print layers/passes of type-2 (region adjacent to the support substrate) had a composition of wt% 50NiO/50YSZ. The next 4 print passes had a composition of wt% 33NiO/67YSZ (4 passes) and the final 4 print passes had a composition of wt% 17NiO/83YSZ. All interlayers covered the entire area of the substrate (1 inch diameter). The printing was carried out using a raster pattern created by AutoCAD® and VMTools™ (VMT) tool paths designed for M³D® system [27]. In type 2, two different drying procedures were adopted. The first drying procedure henceforth called "DP-1" consisted of drying the printed anode interlayer by keeping the platen at room temperature and the second drying procedure henceforth called "DP-2" consisted of drying the interlayer by holding the platen at 60 °C. For type 1, the anode interlayer was dried at room temperature (DP-1 procedure).

2.2. YSZ electrolyte printing

A single pneumatic atomizer was used. In the single atomizer configuration mode, there is no "Y" connection. The atomizer vial was filled with YSZ ink. The ink was atomized using a flow rate of 1500 sccm. A sheath gas flow rate of 3000 sccm was maintained. An exhaust gas flow rate of 1350 sccm was used. Circular areas were filled in by a raster pattern created by AutoCAD® and virtual masking tool [27]. The electrolyte was printed on the dried anode interlayer to cover the entire anode interlayer. The coupons with printed electrolytes were sintered at 1400 °C.

2.3. Cathode and button cell

The SOFC single cell was completed by hand pasting cathode layers on the sintered anode support/anode interlayer/electrolyte coupon. The cathode interlayer, consisting of 50/50 wt% of LSM/YSZ was prepared by ball milling the LSM and YSZ powders, solvents, plasticizer, and dispersant into a highly viscous ink for several hours and then brush painting over the printed electrolyte. The coupon was then sintered at 1200 °C for 1 h. Finally, a cathode current collection layer of LSM paste (NexTech Materials) was brush painted and the cell sintered at 1200 °C.

2.4. Electrochemical testing and low voltage imaging of samples

Silver leads were attached on the cathode and anode sides using gold paste. The cells were then glued onto one end of a ceramic tube using a ceramic paste (Ultratemp 516) and housed in a tube furnace. During characterization of each cell, the furnace was slowly heated to desired temperatures (up to 850 °C) for electrochemical characterization. The anode side was reduced in 5% hydrogen in argon, while the cathode side was exposed to forced
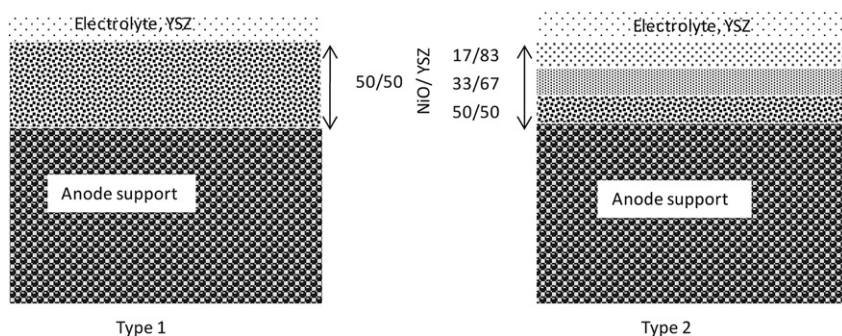

Fig. 2. Schematic of anode interlayer; type 1 − non graded, type 2 − graded interlayer with NiO/YSZ.

air. After reducing for few hours, the anode side was exposed to dry hydrogen at a flow rate of 65 sccm. Button cells were tested for their electrochemical performance. The cell performance was measured using a multi-channel electrochemical test station comprised of a Solartron 1470E potentiostat/galvanostat combined with a Solartron 1450 frequency response analyzer. For electrochemical testing, hydrogen and air were used as fuel and oxidant respectively. After electrochemical testing, the cells were cooled to room temperature with the anode side exposed to a reducing atmosphere of 5% H_2 in Ar. After cooling, the morphology and microstructure were characterized.

Representative samples from different tested cells were collected for analysis by initially shattering the bulk specimens and then selecting an appropriate shard for analysis (e.g. size, shape, intact layered structure, etc.). The shard was then mounted in cross section in Polyfast conductive hot compression mounting material. The mounted specimen was then polished through a schedule of successively finer grit abrasives (SiC papers, diamond suspensions on cloth, and 0.05 micron colloidal silica). The specimen was cleaned in an ultrasonic bath with soap solution between each polishing step. The secondary electron and backscatter electron images were collected with an Everhart–Thornley detector on an FEI Sirion FEG-SEM instrument using a 4Pi image acquisition system. The X-ray data was acquired with an EDAX Genesis/Apollo X SDD-EDS system on an FEI Quanta 600 Mk2 FEG-SEM instrument. Specimens were plasma cleaned prior to imaging and they were not coated with a conductive surface coating.

3. Results and discussion

3.1. Ink characterization, deposition rate, printing and cell performance

Fig. 3 shows the room temperature (23 °C) viscosity plots as a function of shear rate for NiO ink, YSZ ink and the ink vehicle (vehicle consisted of solvents, dispersant and other organic additives but with no active powders). Both YSZ and NiO are seen to be somewhat shear thinning with similar viscosity values at low shear rates up to 200 s^{-1}. A largely Newtonian behavior is observed for YSZ up to 500 s^{-1} with a viscosity of 19.5 mPa s. A shear thickening effect can be seen for further increase in shear rate. Shear

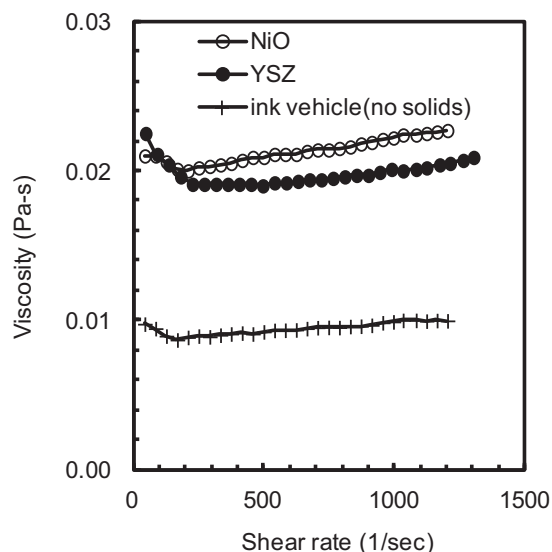thickening effect is also seen for NiO at shear rates $\geq$200 s^{-1} with the viscosity ranging from 20 to 22 mPa s. The shear thinning effect seen for both YSZ and NiO is also seen for the ink vehicle at $\leq$200 s^{-1} and thereafter a slight shear thickening effect similar to NiO is seen. The shear thickening effect seen in these samples appears to arise from the interactions of the polymer components in the inks. The addition of active powders to the ink vehicle increases the viscosity due to interactions of the particles with the polymers.

Deposition rate curves are shown in Fig. 4 for different atomizing gas flow rates, F_{at} = 1000, 1250 and 1500 sccm (air) for NiO and YSZ. For YSZ as well as NiO, the trends in deposition rates are similar; decreasing with increasing exhaust flow in a polynomial fashion. For lower exhaust flow rates (not shown in the plot), i.e., for $F_{ex} < 700$ sccm for F_{at} 1000 sccm, <800 sccm for F_{at} 1150 sccm, and <1200 sccm for F_{at} 1500 sccm, the deposition rates did not follow a polynomial trend, and generally decreased with decreasing exhaust flow rates. It can be seen that YSZ has a higher deposition rate than NiO for all F_{at}. The maximum deposition is 15 mg min^{-1} (wet weight) for YSZ and 12 mg min^{-1} for NiO. This now allows a compositional variation of these two components, NiO and YSZ. After deposition, the samples were dried and the weights measured. There was a weight loss of 15–28% that was consistent for both NiO and YSZ. The weight loss depended on the mist flow rate, where mist flow rate is defined as the difference between atomizer flow and exhaust flow rate. For lower mist flow rates upto ∼150 sccm, the loss was lesser, toward 15%, and for higher mist flow rates, ∼400 sccm, the weight loss was 28%. This difference in weight loss with mist flow rates could imply an unintended role of the virtual impactor in drawing some of the atomized particles during flow reduction. Table 1 shows the selected compositions, and their corresponding gas flow conditions used for the compositional grading shown schematically in Fig. 2. Mist flow rates not exceeding 250 sccm were chosen for the current study. The characteristics of the starting powders, resulting viscosity/dispersion of suspension, surface tension, atomizing conditions (gas flow rates) determine the atomization and resultant deposition rate. Droplets having an optimum size and momentum exit the nozzle. The larger particle size of NiO and higher viscosity are likely some of the contributing factors for the lower deposition rate compared to YSZ. The multi-point BET surface area measurements of the starting powders gave a value of 4.53 m^2 g^{-1} for NiO and 6.98 m^2 g^{-1} for YSZ suggesting a smaller particle size for YSZ.

Fig. 3. Viscosity plots (23 °C) as a function of shear rate for NiO ink, YSZ ink and the ink vehicle.
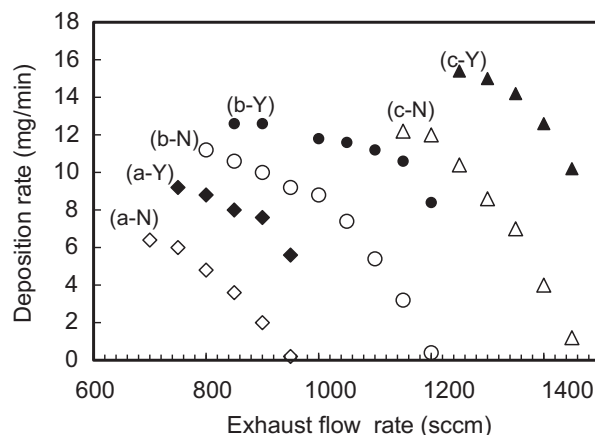

Fig. 4. Deposition rate curves for different atomizing gas (air) flow rates F_{at} for NiO and YSZ inks; a, b, and c denote atomizing flow rate 1000, 1250 and 1500 sccm respectively and Y denotes YSZ, and N denotes NiO. Sheath gas (air) was fixed at 3000 sccm for all depositions.

Table 1
Gas flow conditions for the selected NiO/YSZ compositions in the anode interlayer.

Anode interlayer composition		Gas flow conditions and deposition rates					
		NiO			YSZ		
NiO (wt%)	YSZ (wt%)	Atomizer (sccm)	Exhaust (sccm)	Deposition rate (mg min^{-1})	Atomizer (sccm)	Exhaust (sccm)	Deposition rate (mg min^{-1})
50	50	1000	760	6	1000	940	6
33.3	66.7	1000	840	4	1000	860	8
16.7	83.3	1000	900	2	1250	1160	10
0	100	–	–	0	1250	1000	12

The current–voltage profiles for the button cells at 850 °C are shown in Fig. 5 for both sets: set-1 and set-2. The cells exhibited stable voltages close to 1.20 V. It can be seen from Fig. 5 that cells with a functionally graded anode interlayer (curves b and c) perform better than cells with a non graded interlayer (curve a). The current density is about 500 mA cm^{-2} at maximum power density, 235 mW cm^{-2} for curves b and c in both sets. Curves b and c correspond respectively, to the two different anode interlayer drying procedures, DP-1 and DP-2 described in Section 2.1.3. The two different drying procedures (holding the platen at room temperature, DP-1 and holding the platen at 60 °C, DP-2) do not have an impact on the cell performance. The maximum power density for curve a is 200 mW cm^{-2} in both sets. Although all cells exhibited an overall low performance, these results very clearly elucidate the advantage of functionally graded structures as well as the reproducibility of the current printing method.

3.2. Low voltage scanning electron microscopy – evaluation of material mixing

Imaging Ni and YSZ phases SOFC anode can be challenging given that Ni (percolating and non-percolating), YSZ and void density are
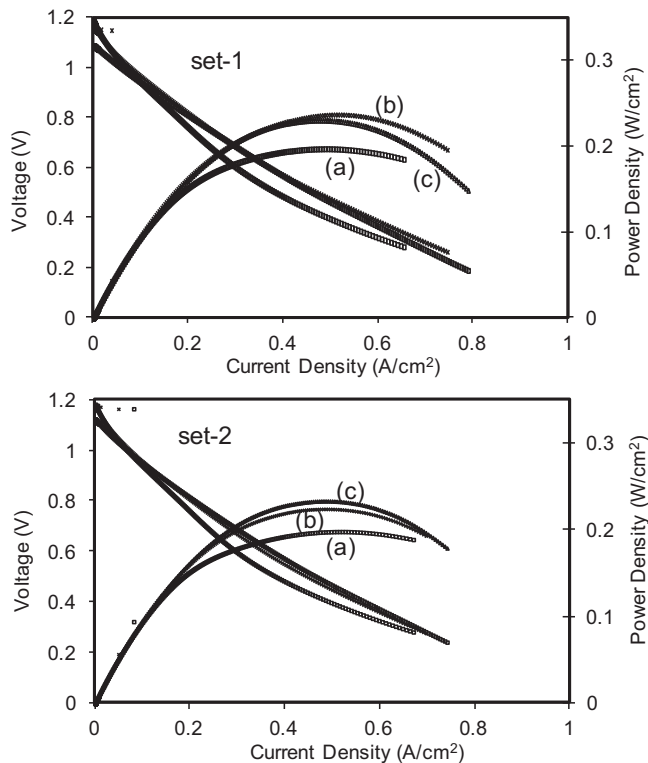
Fig. 5. Current–voltage profiles at 850 °C for two identical sets of cells; (a) non graded anode interlayer, (b) functionally graded anode interlayer with DP-1 drying procedure and (c) functionally graded anode interlayer with DP-2 drying procedure.

difficult to clearly distinguish. First, the inability of back scattered electrons (BSE) to discern between percolating nickel and non-percolating Ni due to the lack of Z-contrast (atomic number contrast) prohibits distinction between them, and secondly, the nearly identical backscatter coefficient possessed by nickel and the YSZ phases (no Z-contrast in the backscatter signal) renders difficult, the distinction between Ni and YSZ. Characteristic X-ray signals (e.g. EDS mapping) used for imaging can be used to differentiate between the Nickel and the YSZ phase, but the technique takes a prohibitively long time to acquire an image that would have a signal to noise level and pixel resolution approaching those typically found in an electron image. Also, like BSE Z-contrast imaging, X-ray mapping cannot differentiate between percolating and non-percolating nickel. Thydén et al. [31] proposed a solution to this problem by using low-voltage secondary electron (SE) imaging. At accelerating voltages typically used for SEM imaging, the backscatter coefficient of most materials is nominally independent of the accelerating voltage. However, at low accelerating voltages (<5 kV), there can be a measurable dependence of the backscatter coefficient on the accelerating voltage (and therefore the secondary electron signal will vary as well, i.e. SE II and SE III signals. SE II is the secondary electron signal generated by the outgoing BSE, and SE III is the secondary electron signal generated by BSE impacting the pole piece and chamber). According to Thydén et al., there is a divergence of the YSZ and Ni backscatter coefficients in the low-voltage regime. This trend can be substantiated by using the following empirical expressions that were developed for estimating the backscatter coefficient, as shown by Goldstein et al. [32],

$$\eta(Z,E) = E^m C$$

$$m = 0.1382 - \frac{0.9211}{Z^{1/2}}$$

$$C = 0.1904 - 0.2235(\ln Z) + 0.1292(\ln Z)^2 - 0.01491(\ln Z)^3 \quad (1)$$

where Z is atomic number, E is accelerating voltage, and η is the backscatter coefficient of particular elemental species corresponding to Z.

The backscatter coefficient of YSZ can be approximated by the application of a rule of mixtures to the calculated backscatter coefficients that are determined for each of the constituent atomic species [32].

$$\eta = \sum_i C_i \eta_i \quad (2)$$

where η_i is the backscatter coefficient of the pure element and C_i is the weight concentration of element i.

The contrast between the two phases can then be estimated as

$$\text{Contrast}(\%) = 100 * (\eta_{Ni} - \eta_{YSZ})/\eta_{Ni} \quad (3)$$

Thus, by imaging at low voltages, it should be possible to differentiate between nickel and YSZ phases in both the secondary

(because of SE II and SE III signal) and the backscatter imaging modes. Further, by using a conductive mounting material, the percolating nickel will not accumulate charge under the influence of the electron beam. The same is not true for the non-percolating nickel, which will accumulate a charge during imaging. The conductivity difference between the two nickel phases thus provides a means for generating a contrast difference between the percolating and the non-percolating nickel. Fig. 6a provides an example of the contrast that is observed between the YSZ and the Ni when imaging at 1 keV. The imaged area is from the anode substrate. Note the contrast difference between the percolating (bright white regions) and the non-percolating nickel, as indicated by the highlight boxes. Fig. 6b shows the X-ray imaging used to confirm the identity of the phases found in the secondary electron image. Green regions correspond to Ni and blue regions correspond to YSZ. Black highlight boxes indicate the locations of some non-percolating Ni. Phase morphology was also found to be helpful in identifying the different phases more quickly, once successful low-voltage images were collected. It was determined that the specimens required plasma cleaning prior to imaging in order to prevent the build-up of carbon under the incident electron beam during imaging. The deposition of carbon under the influence of the electron beam significantly reduced the observed contrast that was generated between the different phases (For interpretation of the references to color in this paragraph, the reader is referred to the web version of this article.).

Generally, as the primary beam energy is reduced, the electron penetration range falls rapidly and the stopping power increases. The result is that secondary electron yield increases as accelerating voltage decreases [33,34]. Further, since the earliest days of SEM, it has been expected that the secondary electron yield (SE I, the SE signal generated by the primary electrons of the incident beam) will vary with specimen composition (i.e. Z-contrast can arise in the secondary electron image that is independent of the backscatter signal), although this has been difficult to realize in practice [33]. Thus, one has to wonder if the contrast being observed in the SOFC anode materials at low-voltage is genuinely arising from the proposed BSE mechanism. In an effort to make this determination, it was decided to isolate the BSE signal from the SE signal and observe the resulting image contrast.

The Everhart–Thornley detector (ETD), when operated with a positive bias, efficiently collects the secondary electron signal, constituted by the many components, SE I, SE II, SE III, SE IV. SE IV is the secondary electrons generated at the final aperture and line of sight back scattered electrons. Thus, a major component of the secondary electron signal collected by the ETD is dependent upon the magnitude of the back scattered electron signal, so the ETD cannot be used to isolate a pure SE I signal. However, negatively biasing the ETD provides a way to reject the secondary electron signal, thereby isolating and collecting the line-of-sight BSE signal generated during low-voltage imaging (1 keV). While a typical solid-state diode backscatter detector can detect the contrast generated by a 0.1Z difference, the minimum BSE contrast detectable by the negatively biased ETD was not known at the outset of the current work. By imaging a duplex brass standard specimen having a known 0.1Z difference, under the identical conditions used to image the sample anode materials, it was confirmed that the negatively biased ETD could be used to successfully observe even 0.1Z difference at 1 keV primary beam energy.

Fig. 7 shows the results of an imaging experiment on a sample of the anode substrate, wherein the energy of the primary imaging electrons was systematically lowered from 30 keV to 1 keV. Except for the one image indicated as otherwise (see figure caption), all of the images in this voltage series were acquired with a negatively biased ETD so as to collect a pure BSE image. Note that the Z-contrast is essentially absent from all of the images except for the two images that were collected at 1 keV. The image set provided in Fig. 7 thus confirms that the BSE contrast mechanism proposed by Thydén et al. is active at 1 keV. Thus given that the proposed contrast mechanism is due to variation in the BSE signal, it is interesting to note that experiments on carbon coated and non-coated specimens have shown that carbon coating the specimen will prevent this contrast from being observed. Unfortunately for the present discussion, it was not possible to collect a pure SE I signal with the equipment that was available (all SE images collected will have a BSE related component). Thus, one cannot say in a quantitative sense the extent to which the observed low-voltage contrast in the anode materials is due to variation in the BSE signal vs. variation in the SE I signal.

Fig. 8 shows the low voltage SEI of the cross-section of the electrochemically tested cells (type-1 and type-2 of one set with

5 μm
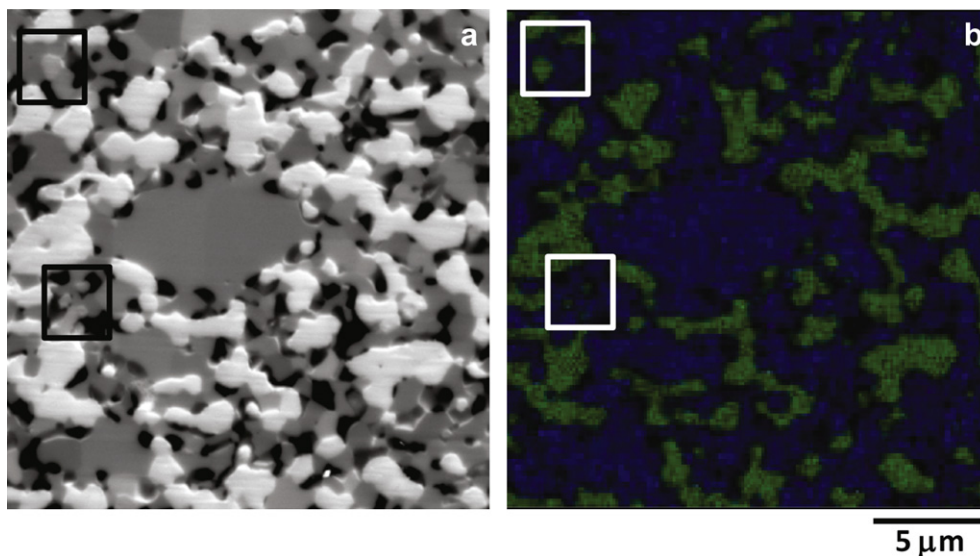
Fig. 6. a) Low voltage SEM image of specimen sample in the anode substrate (1 kV, SEI, ETD (bias +300 V)). b) Phase identification map constructed from qualitative X-ray microanalysis data (green = Ni Blue = YSZ). Black highlight boxes indicate the locations of some non-percolating Ni. Bright white regions correspond to percolating nickel (For interpretation of the references to color in this figure legend, the reader is referred to the web version of this article.).
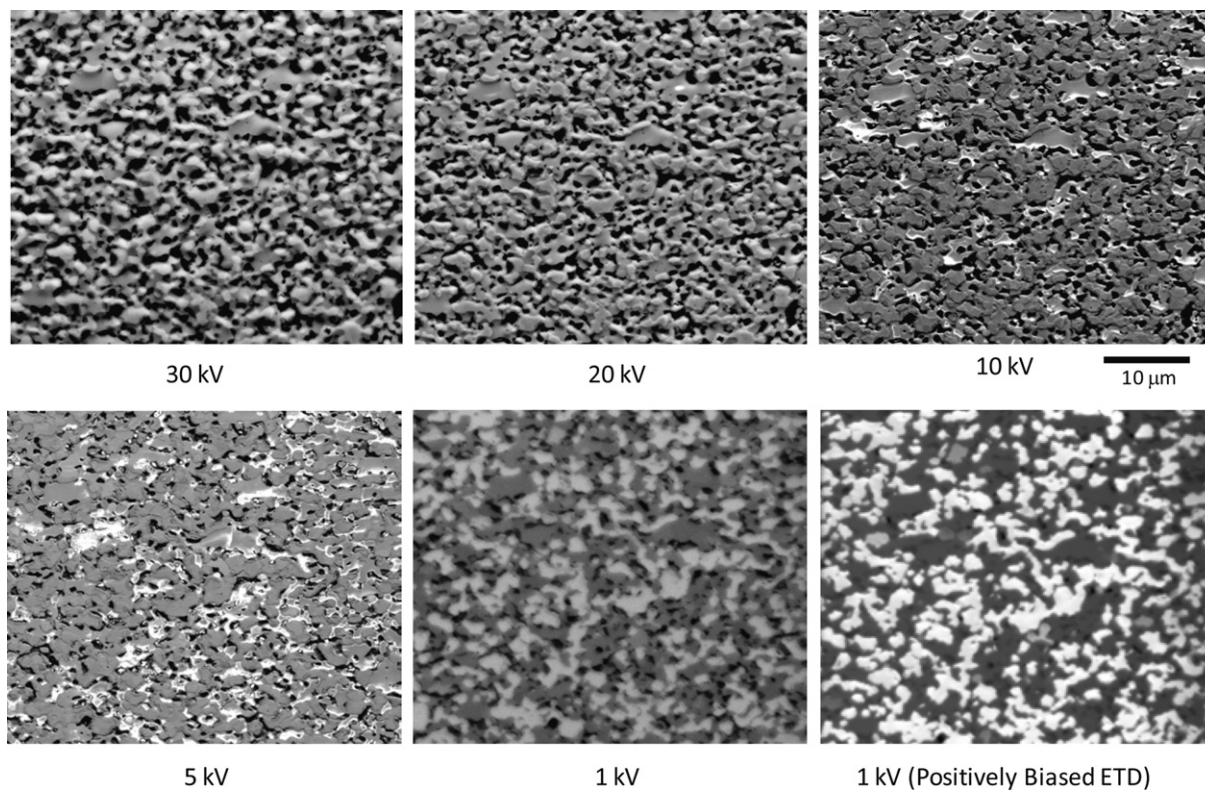
Fig. 7. Fixed specimen region in the anode substrate imaged at different accelerating voltages (negatively biased ETD, except where indicated).

DP-1 drying procedure) whose anode interlayer design scheme is shown in Fig. 2 and electrochemical performance is shown in Fig. 5. The magnified interlayer region is shown below each of the cell for clarity. These images reiterate the reproducibility in layer thickness and microstructure. Both type 1 and type 2 cells have similar electrolyte and anode interlayer thicknesses. The electrolyte is dense and 12 μm in thickness. Both anode interlayers are 35 μm thick. In type 1, a uniform distribution of Ni and YSZ is seen, while
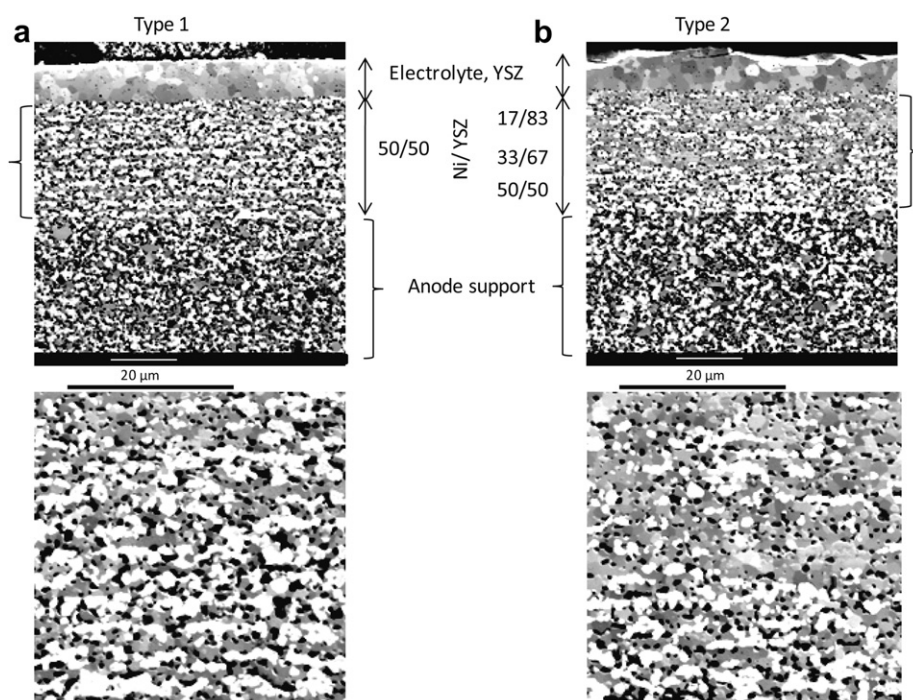
Fig. 8. Low voltage SEM (1 kV) image of the cross-section of the electrochemically tested cells (type-1 and type-2 of set-1 with DP-1 drying procedure) whose anode interlayer design scheme is shown in Fig. 2 and electrochemical performance is shown in Fig. 5.

a gradation can be readily seen in type 2. On comparing the magnified images of the graded and non-graded layers, it can be seen that the volume fraction of YSZ relative to Ni in the graded interlayer is larger in the region adjacent to the electrolyte compared to regions closer to the anode support. The consequent decrease in ohmic drop in the electrode has likely resulted in the enhanced electrochemical performance. It is also likely that the lesser amount of Ni in the region adjacent to the electrolyte, is below the threshold for conductivity based on percolation theory [35]. Typically below this threshold, which is 30 vol%, the cermet exhibits predominantly ionic conducting behavior resulting in a reduction in ohmic resistance in the region adjacent to the electrolyte in the graded interlayer that is absent in the non-graded interlayer and thus contributes to the enhancement in electrochemical performance. However, in the non-graded interlayer as well as the lower region adjacent to the electrolyte in the graded interlayer, a layering effect can be seen in the interlayer region, with features similar to striations of Ni and YSZ suggesting either inhomogeneous mixing of NiO and YSZ before reaching the deposition head or a de-mixing of the two phases on its transit from the deposition nozzle to the substrate due to differences in density. This factor together with sub optimized layer thickness, porosity and contiguity likely contribute to the overall less than satisfactory performance of the cells. It is also likely that a large part of the nickel is non-percolating. Clearly, further optimization of the anode interlayer is required. Optimizations could include, among others, a modification of the thickness of the anode interlayer, quantifying the final composition in the interlayer, modifying the viscosities of the individual inks and changing the nozzle to substrate distance. Composite cathode layers studied in earlier work [28] presented no mixing/de-mixing issues, and the electrochemical performance of cells with printed composite cathode showed comparable performance to those fabricated by slurry pasting. This implies processing and ink optimization issues rather than printing issues. This preliminary work on graded composite layers using aerosol jet printing method shows the potential advantages in terms of electrochemical performance of functionally graded anode structures over non-graded structures. Similar results of performance enhancement in sub optimized cells have been observed by other groups, who used graded porosity in tape cast anode supported cells [36]. Cells with graded anode performed better than cells without the graded layer. A power density of 101 mW cm^{-2} was observed for their cells at 600 °C. The results of the current work also reiterate the reproducibility of component structures and hence electrochemical performance in cells fabricated by direct write methods. While this preliminary study on compositional grading using dual atomizers has provided a platform for fabricating functionally graded materials, detailed studies quantifying the final compositions etc. are required and will be the topic of future work.

4. Conclusion

YSZ electrolyte and compositionally graded composite anode interlayers were printed by aerosol jet printing from individual components of NiO and YSZ suspensions. The AJP (Aerosol Jet® Printing) system's dual atomizer configuration that allows on-demand material mixing was used to deposit the composite NiO/YSZ interlayer component. These electrolyte and anode functional layers together with a standard LSM (strontium doped lanthanum manganite) based pasted cathode layer were deposited onto anode supported SOFC button cell. Cells with compositionally graded anode interlayers performed better than cells with a non-graded anode interlayer. The enhancement in electrochemical performance was very consistent and reproducible and can be attributed

to the functional gradation with respect to composition. The microstructure in the graded anode interlayer shows a larger volume fraction of YSZ relative to Ni in the region adjacent to the electrolyte compared to regions closer to the anode support, leading to a reduced ohmic resistance, and hence better electrochemical performance compared to cells with non graded interlayer where there is a uniform distribution of Ni and YSZ. However, the overall performance of all cells was not satisfactory, and requires further optimization of the anode interlayer by altering the ink characteristics. Issues relating to improper mixing before reaching the deposition head or de-mixing of the aerosolized suspension on its transit from the nozzle to the substrate requires closer examination. Low voltage scanning electron microscopy was used to characterize the printed layers. The use of low accelerating voltages (<5 kV) introduces a divergence in the backscattering coefficients of YSZ and Ni and enables very clear distinction of the phases, not obtainable with routine scanning electron microscopy using 10—20 kV. The backscattering mechanism responsible for image contrast was confirmed and clarified by specially designed SEM experiments that isolated BSE (back scattered electrons) from SE (secondary electrons).

From the results of the study on microstructural and electrochemical performance of button cells, it is clear that the current printing method of fabricating SOFC layers has advantages of high reproducibility. For SOFC and other applications where component thicknesses ranging from a few microns to tens of microns, where both porous and dense layers are required, and/or complex multi-layer designs such as the segmented in series cells requiring both thickness and spatial control, aerosol jet printing method offers great potential as a viable manufacturing method.

References

[1] N. Minh, J. Am. Ceram. Soc. 76 (1993) 563—588.
[2] S. Singhal, Solid State Ionics 135 (1—4) (2000) 305—313.
[3] A.O. Isenberg, Solid State Ionics 3/4 (1981) 431—437.
[4] J. Will, A. Mitterdorfer, C. Kleinlogel, D. Perednis, L.J. Gauckler, Solid State Ionics 131 (1—2) (2000) 79—96.
[5] F. Teitz, H.P. Buchkremer, D. Stover, Solid State Ionics 152—153 (2002) 373—381.
[6] L.R. Pederson, P. Singh, X.D. Zhou, Vacuum 80 (10) (2006) 1066—1083.
[7] A. Negishi, K. Nozaki, T. Ozawa, Solid State Ionics 3/4 (1981) 443.
[8] A. Nagata, H. Okayama, Vacuum 66 (2002) 523—529.
[9] X. Chen, N.J. Wu, D.L. Ritums, A. Ignatiev, Thin Solid Films 342 (1—2) (1999) 61—66.
[10] T. Franco, Z. Hoshiardin, P. Szabo, M. Lang, G. Schiller, J. Fuel Cell. Sci. Technol. 4 (4) (2007) 406—412.
[11] G. Schiller, R.H. Henne, M. Lang, R. Ruckdäschel, S. Schaper, Fuel Cells Bull. 3 (21) (2000) 7—12.
[12] R. Hui, Z. Wang, O. Kesler, L. Rose, J. Jankovic, S. Yick, R. Maric, D. Ghosh, J. Power Sources 170 (2007) 308—323.
[13] S.C. Singhal, in: S.C. Singhal, M. Dokiya (Eds.), Proc. 6th Int. Symp. Solid Oxide Fuel Cells (SOFC-VI), The Electrochemical Society, Pennington, NJ, 1999. p. 39.
[14] D. Simwonis, H. Thülen, F.J. Dias, A. Naoumidis, D. Stöver, J. Mater. Process. Technol. 92—93 (1999) 107—111.
[15] N. Maffei, G. de Silveira, Solid State Ionics 159 (3—4) (2003) 209—216.

[16] D. Rotureau, J.-P. Viricelle, C. Pijolat, N. Caillol, M. Pijolat, J. Eur. Ceram. Soc. 25 (2005) 2633–2636.
[17] Y. Zhang, J. Gao, G. Meng, X. Lin, J. Appl. Electrochem. 34 (6) (2004) 637–641.
[18] E. Schüller, R. Vaßen, D. Stöver, Adv. Eng. Mater. 4 (9) (2002) 659–662.
[19] T.W. Kueper, S.J. Visco, L.C. De Jonghe, Solid State Ionics 52 (1992) 251.
[20] S. De Souza, S.J. Visco, L.C. De Jonghe, Solid State Ionics 98 (1–2) (1997) 57–61.
[21] D. Young, A.M. Sukeshini, R. Cummins, H. Xiao, M. Rottmayer, T. Reitz, J. Power Sources 184 (2008) 191–196.
[22] A.M. El -Toni, T. Yamaguchi, S. Shimizu, Y. Fujishiro, M. Awano, J. Am. Ceram. Soc. 91 (2008) 346–349.
[23] A.M. Sukeshini, R. Cummins, T.L. Reitz, R.M. Miller, Electrochem. Solid-State Lett. 12 (2009) B176–B179.
[24] A.M. Sukeshini, R. Cummins, T.L. Reitz, R.M. Miller, J. Am. Ceram Soc. 92 (12) (2009) 2913–2919.
[25] R.I. Tomov, M. Krauz, J. Jewulski, S.C. Hopkins, J.R. Kluczowski, D.M. Glowacka, B.A. Glowacki, J. Power Sources 195 (21) (2010) 7160–7167.
[26] N. Yashiro, T. Usui, K. Kikuta, J. Eur. Ceram. Soc. 30 (2010) 2093–2098.
[27] A.M. Sukeshini, P. Gardner, T. Jenkins, T.L. Reitz, R.M. Miller, Proceedings of the ASME 8th International Conference on Fuel Cell Science, Engineering and Technology, vol. 1, Brooklyn, NY, 2010, pp. 325–332.
[28] A. Sukeshini, P. Gardner, F. Meisenkothen, T. Jenkins, R. Miller, M. Rottmayer, T.L. Reitz, ECS Trans. 35 (2011) 2151–2160.
[29] http://www.optomec.com.
[30] N.T. Hart, N.P. Brandon, M.J. Day, J.E. Shemilt, J. Mater. Sci. 36 (2001) 1077.
[31] K. Thydén, Y.L. Liu, J.B. Bilde-Sørensen, Solid State Ionics 178 (39–40) (2008) 1984–1989.
[32] J.I. Goldstein, D.E. Newbury, P.E. Echlin, D.C. Joy, A.D. Romig, C.E. Lyman, C.E. Fiori, E. Lifshin, Scanning Electron Microscopy and X-ray Microanalysis, second ed., Plenum Press, New York, 1992.
[33] D.C. Joy, C.S. Joy, Micron 27 (1996) 247–263.
[34] L. Reimer, Image Formation in Low-voltage Scanning Electron Microscopy, SPIE – The International Society for Optical Engineering, Washington, 1993.
[35] D.W. Dees, T.E. Clair, T.E. Easler, D.C. Fee, F.C. Mrazek, J. Electrochem. Soc. 134 (1887) 2141.
[36] C.M. An, J.H. Song, I. Kang, N. Sammes, J. Power Sources 195 (3) (2010) 821–824.